



**HAL**  
open science

## Using a micro-device with a deformable ceiling to probe stiffness heterogeneities within 3D cell aggregates

Shreyansh Jain, Hiba Belkadi, Arthur Michaut, Sébastien Sart, Jérôme Gros, Martin Genet, Charles N Baroud

► **To cite this version:**

Shreyansh Jain, Hiba Belkadi, Arthur Michaut, Sébastien Sart, Jérôme Gros, et al.. Using a micro-device with a deformable ceiling to probe stiffness heterogeneities within 3D cell aggregates. *Biofabrication*, 2024, 16 (3), pp.035010. 10.1088/1758-5090/ad30c7 . pasteur-04876798

**HAL Id: pasteur-04876798**

**<https://pasteur.hal.science/pasteur-04876798v1>**

Submitted on 9 Jan 2025

**HAL** is a multi-disciplinary open access archive for the deposit and dissemination of scientific research documents, whether they are published or not. The documents may come from teaching and research institutions in France or abroad, or from public or private research centers.

L'archive ouverte pluridisciplinaire **HAL**, est destinée au dépôt et à la diffusion de documents scientifiques de niveau recherche, publiés ou non, émanant des établissements d'enseignement et de recherche français ou étrangers, des laboratoires publics ou privés.



Distributed under a Creative Commons Attribution 4.0 International License

# Biofabrication



## PAPER

### OPEN ACCESS

RECEIVED  
11 October 2023

REVISED  
18 February 2024

ACCEPTED FOR PUBLICATION  
6 March 2024

PUBLISHED  
15 April 2024

Original Content from  
this work may be used  
under the terms of the  
[Creative Commons  
Attribution 4.0 licence](#).

Any further distribution  
of this work must  
maintain attribution to  
the author(s) and the title  
of the work, journal  
citation and DOI.



## Using a micro-device with a deformable ceiling to probe stiffness heterogeneities within 3D cell aggregates

Shreyansh Jain<sup>1,2,6,\*</sup> , Hiba Belkadi<sup>1,2,6</sup> , Arthur Michaut<sup>3</sup> , Sébastien Sart<sup>1,2</sup> , Jérôme Gros<sup>3</sup> ,  
Martin Genet<sup>4,5</sup> and Charles N Baroud<sup>1,2,\*</sup>

<sup>1</sup> Institut Pasteur, Université Paris Cité, Physical Microfluidics and Bioengineering, 25-28 Rue du Dr Roux, 75015 Paris, France

<sup>2</sup> Laboratoire d'Hydrodynamique (LadHyX), CNRS, Ecole Polytechnique, Institut Polytechnique de Paris, 91128 Palaiseau, France

<sup>3</sup> Institut Pasteur, Université Paris Cité, Dynamic Regulation of Morphogenesis, 25-28 Rue du Dr Roux, 75015 Paris, France

<sup>4</sup> Laboratoire de Mécanique des Solides, CNRS, École Polytechnique, Institut Polytechnique de Paris, 91128 Palaiseau, France

<sup>5</sup> Inria, Palaiseau, France

<sup>6</sup> Co-first authors.

\* Authors to whom any correspondence should be addressed.

E-mail: [shreyansh.mechanical@gmail.com](mailto:shreyansh.mechanical@gmail.com) and [charles.baroud@polytechnique.edu](mailto:charles.baroud@polytechnique.edu)

**Keywords:** microfluidics, mechanics, multicellular aggregates, spheroid

Supplementary material for this article is available [online](#)

### Abstract

Recent advances in the field of mechanobiology have led to the development of methods to characterise single-cell or monolayer mechanical properties and link them to their functional behaviour. However, there remains a strong need to establish this link for three-dimensional (3D) multicellular aggregates, which better mimic tissue function. Here we present a platform to actuate and observe many such aggregates within one deformable micro-device. The platform consists of a single polydimethylsiloxane piece cast on a 3D-printed mould and bonded to a glass slide or coverslip. It consists of a chamber containing cell spheroids, which is adjacent to air cavities that are fluidically independent. Controlling the air pressure in these air cavities leads to a vertical displacement of the chamber's ceiling. The device can be used in static or dynamic modes over time scales of seconds to hours, with displacement amplitudes from a few  $\mu\text{m}$  to several tens of microns. Further, we show how the compression protocols can be used to obtain measurements of stiffness heterogeneities within individual co-culture spheroids, by comparing image correlations of spheroids at different levels of compression with finite element simulations. The labelling of the cells and their cytoskeleton is combined with image correlation methods to relate the structure of the co-culture spheroid with its mechanical properties at different locations. The device is compatible with various microscopy techniques, including confocal microscopy, which can be used to observe the displacements and rearrangements of single cells and neighbourhoods within the aggregate. The complete experimental and imaging platform can now be used to provide multi-scale measurements that link single-cell behaviour with the global mechanical response of the aggregates.

## 1. Introduction

The field of mechanobiology has experienced rapid growth in recent years, both from a fundamental science point of view [1] and for tissue engineering applications [2]. This growing interest in the link between mechanics and biology has led to the development of a wide range of techniques to measure the elastic and viscoelastic properties of individual cells, including atomic force microscopy, optical stretchers,

microfluidics, or deformable pillars [3]. As a result, the mechanical properties of cells can now be related to their state of disease [4, 5] or their differentiation potential [6], while mechanical cues are used to direct stem cell differentiation [7] or to induce an epithelial to mesenchymal transition of cancer cells [8]. Beyond work on individual cells, collective phenomena have also been studied on two-dimensional (2D) monolayers of cells, e.g. using traction force microscopy or image analysis [9–11].

In contrast with this highly developed field, very few methods have been able to measure the elastic or viscoelastic (the rheological) properties of 3D tissues. This is a strong limitation since three-dimensional (3D) tissues recapitulate the mechanics and biology *in vivo*. Some work has probed the forces acting within growing 3D tissues [12–15], while different methods have been devised to measure the rheology of individual spheroids [16–18]. However, there is a need for a simple method that can probe the spheroid mechanobiology dynamically and generate data on multiple spheroids in parallel.

The mechanical manipulation of multiple cellular monolayers (2.5D) or 3D cellular aggregates has been performed using several microfluidic platforms, either through the stretching of a membrane [19] or the 3D compression of multicellular spheroids in a hydrogel [20]. These methods leverage the flexibility of the most common microfluidic material, polydimethylsiloxane (PDMS), to apply deformations or stresses on the biological structure. In both of these approaches, the pressure is controlled inside air-filled chambers that are positioned on the sides of the channel containing the biological material. The deformation of these chambers applies a lateral motion in the plane of the device, which is then transferred to the biological tissue through a flexible membrane [19] or a hydrogel [20]. A consequence of this choice is that the micro-fabrication requires either multi-layered devices or thin membranes that must be bonded to the glass substrate.

Here we introduce an alternative approach to studying the mechanics of 3D cultures, based on using out-of-plane deformations of the microfluidic device. The geometry, which is inspired by recent advances in the field of soft robotics [21], is simple to fabricate in a single PDMS casting step on a 3D printed mould. We show that the devices can produce well-calibrated static or dynamic loads on cell spheroids, over periods of a few seconds to several hours. Further, we also show how mechanical information about the cell state can be extracted by comparing measurements obtained from bright-field imaging with numerical simulations. Finally, we show that the device is suitable for high-resolution confocal microscopy, which opens the path to linking single-cell with tissue-level behaviours.

## 2. Microfluidic design and characterisation

The microfluidic design is based on immobilising spheroids between the roof and floor of a wide (in-plane) and flat (out-of-plane) *observation chamber* and then applying compressive forces by modulating the height of this chamber. The construction of the chamber then allows unhindered optical access to the spheroid shape and other optical measurements during the mechanical compression, as described below.

### 2.1. Chip geometry and fabrication protocol

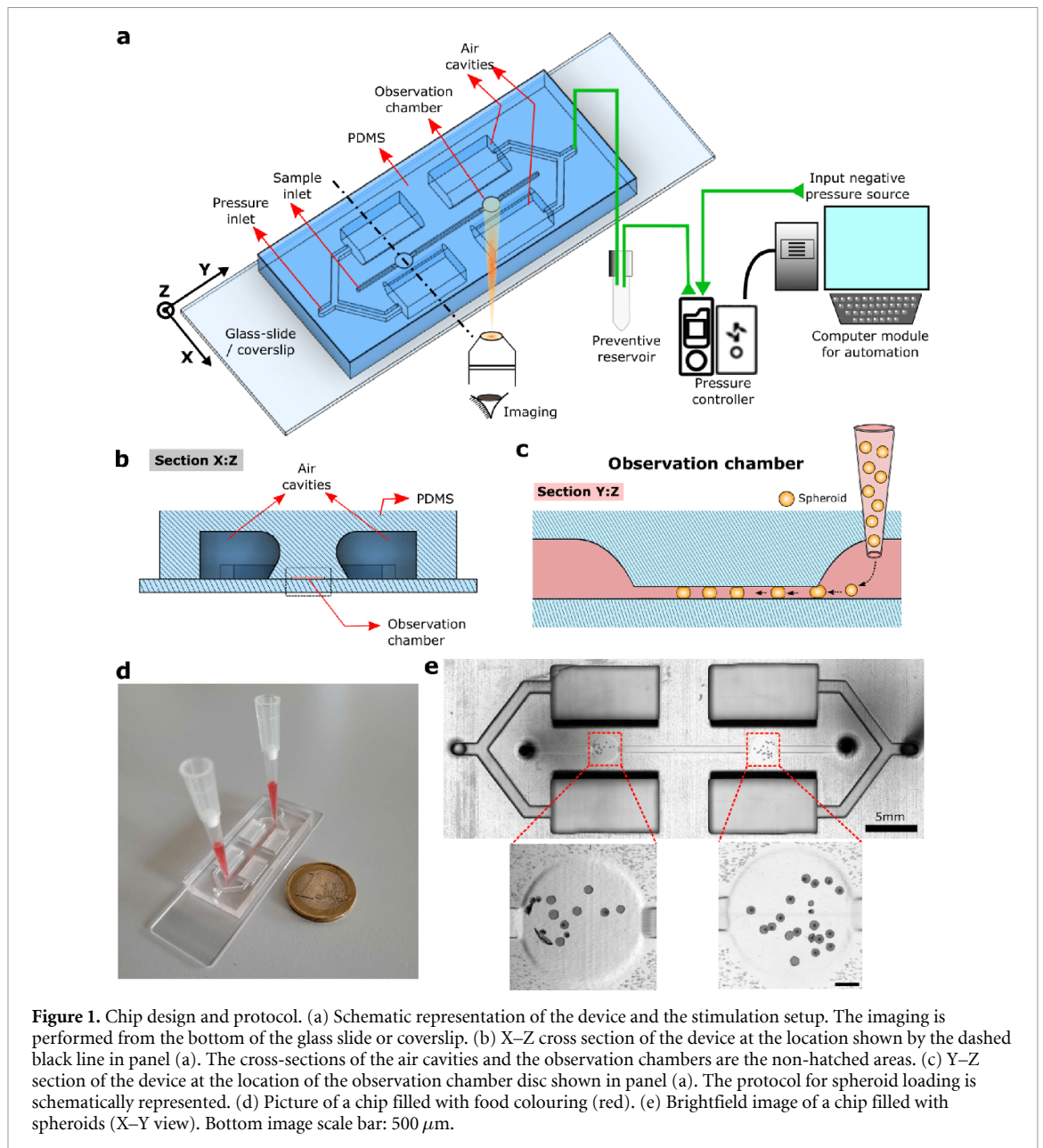
The micro-device is fabricated as a monolithic piece of PDMS, which is cast onto a 3D-printed mould, then bonded to a coverslip or glass slide. It is composed of two main components, as shown in figure 1(a): two observation chambers that are surrounded by two air cavities each. The observation chambers contain the spheroids and are fluidically independent of the air cavities (see cross-section in figure 1(b)). Each of the two observation chambers is a disc of diameter 2.5 mm and height 100  $\mu\text{m}$ . They are connected to each other and to the channel inlets with a 500  $\mu\text{m}$  high channel, as shown in the cross-section of figure 1(c) and the full scan of the device in figure 1(e). Two air cavities surround each observation chamber. They are rectangular in the  $x$ - $y$  plane and have a right-trapezoidal cross-section, with one rounded corner, in the  $x$ - $z$  plane (figure 1(b)). Applying a negative pressure inside the air cavities deforms the PDMS and decreases the ceiling height in the observation chamber, allowing for the compression of the spheroids.

A typical experiment begins with filling the observation chamber with the culture medium. Then preformed hepatoma and/or fibroblast spheroids ( $130 \pm 20 \mu\text{m}$  in diameter) are introduced at the inlet, using a hand-held pipette. The high ceiling of the channel allows them to flow freely at first. Once they reach the observation chamber they are slightly compressed, so that they become trapped by the low ceiling (figure 1(c)). The spheroids can then be deformed by the moving ceiling, while their geometrical and functional responses are observed with a microscope (figure 1(e)).

### 2.2. Calibration of the ceiling deformations

Applying a negative pressure inside the air cavities deforms the device and decreases the ceiling height in the observation chamber. This deformation depends on the geometry and inner pressure of the air cavities. To control the strain applied to the spheroids, the device deformation is calibrated for different inlet pressures, as shown in figure 2.

First, the device deformation was simulated using Autodesk Fusion 360 for different geometries of the air cavities and observation chambers (figures 2(a)–(c) and SI movie 1 for an animation). A rounded trapezoidal cross-section of the air cavities was found to induce an efficient vertical displacement of the ceiling of the observation channel, for the range of negative pressures available. In particular, the protrusion of the overhanging part above the channel could be modulated to enhance the deformation of the observation chamber. The amount of protrusion was then chosen through a compromise between increasing the deformation while maintaining the ease of microfabrication, particularly when peeling the PDMS off the 3D-printed mould.

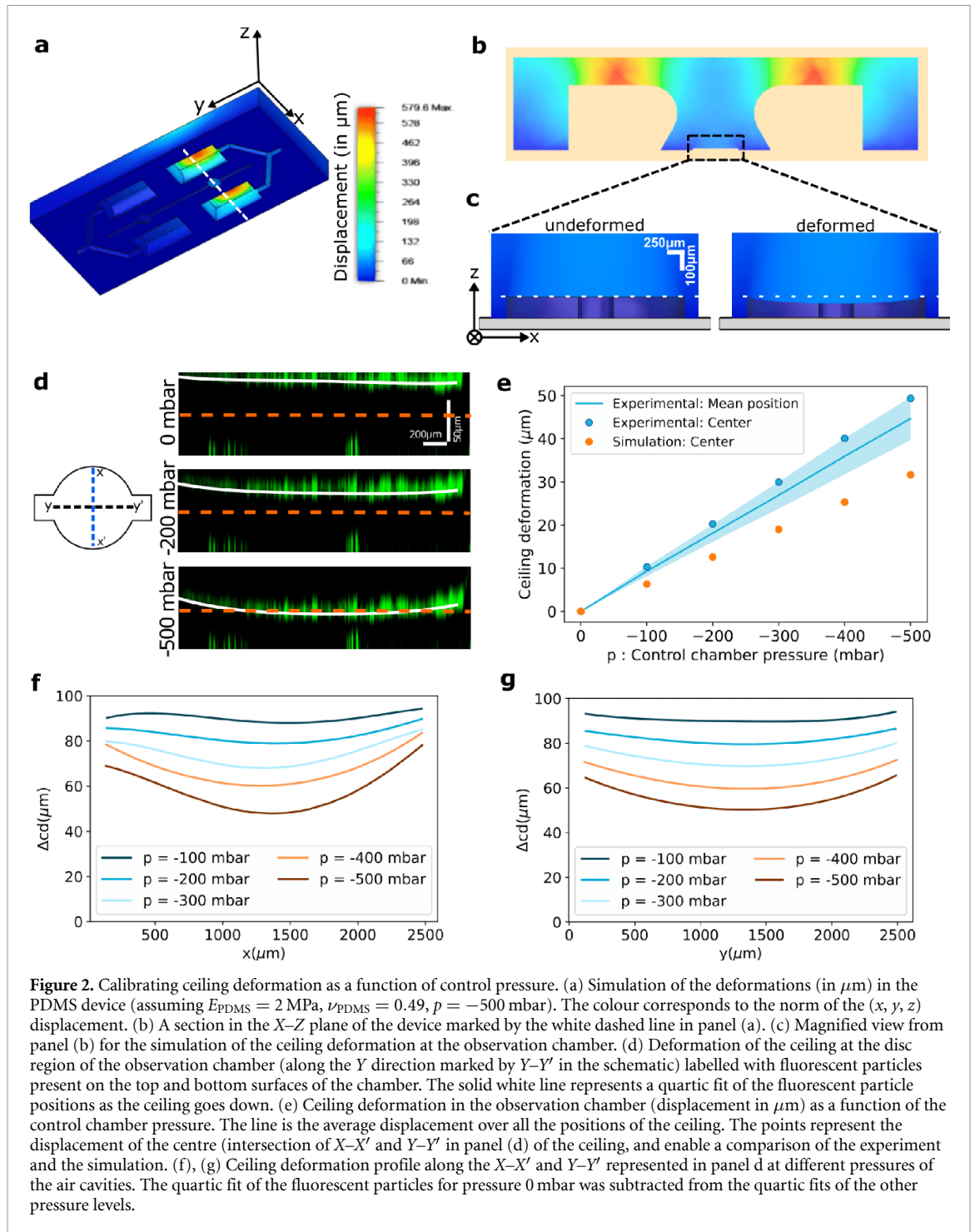


The simulation results were then tested experimentally by injecting a suspension of fluorescent microspheres into a device and letting the solvent dry. This led the PDMS and glass surfaces inside the chip to be non-specifically coated with a layer of fluorescent particles that could be tracked by performing confocal  $z$ -stacks for different air cavity pressures, as shown in the orthogonal views along  $y$ – $y'$  in figure 2(d) (SI movie 2). They show that the whole ceiling indeed goes down as negative pressures are applied in the air cavities. It is important to notice that the axes in these images are scaled unequally, as is apparent from the scale bars. The ceiling is, therefore, essentially flat and curves slowly around the edges. The ceiling position is then estimated by fitting a quartic function (in white) to the positions of the fluorescent particles. Then by subtracting the fit at

zero applied pressure, the vertical displacement of the ceiling could be measured at each pressure.

The experimental measurements show that the vertical displacement of the ceiling increases linearly as a function of the negative pressure, independently of the position within the chamber figure 2(e). To compare simulation and experiments, the displacement of the chamber centre is shown for each case. The simulation also predicts a linear displacement of the chamber centre but underestimates its value by  $\approx 1/3$ .

The profiles of the ceiling along  $x$ – $x'$  and  $y$ – $y'$  are shown in figures 2(f) and (g), for a moderate range of pressures. Over this range, the variability in the ceiling displacement over its surface is  $\approx \pm 10\%$  around the mean value. Note that it is possible to entirely collapse the ceiling by extending the pressure range.



### 2.3. Applying static and cyclic compression on spheroids

By following the protocols above, multiple spheroids can be injected into the observation chamber with a pipette. They can then be deformed in parallel while being observed with brightfield microscopy, as shown in figures 3(a) and (d) and supplementary movie 3 for spheroids formed from a hepatoma cell line (H4-II-EC3). Since the pressure

in the air cavities is computer-controlled, it is possible to program the spheroids to be compressed either statically, see figures 3(a)–(c), or dynamically, see figures 3(d)–(f). As the spheroids are compressed vertically and observed from the bottom, their area increases in the brightfield images. The spheroids are segmented automatically (figure 3(e)) and the change in their equatorial area is monitored.



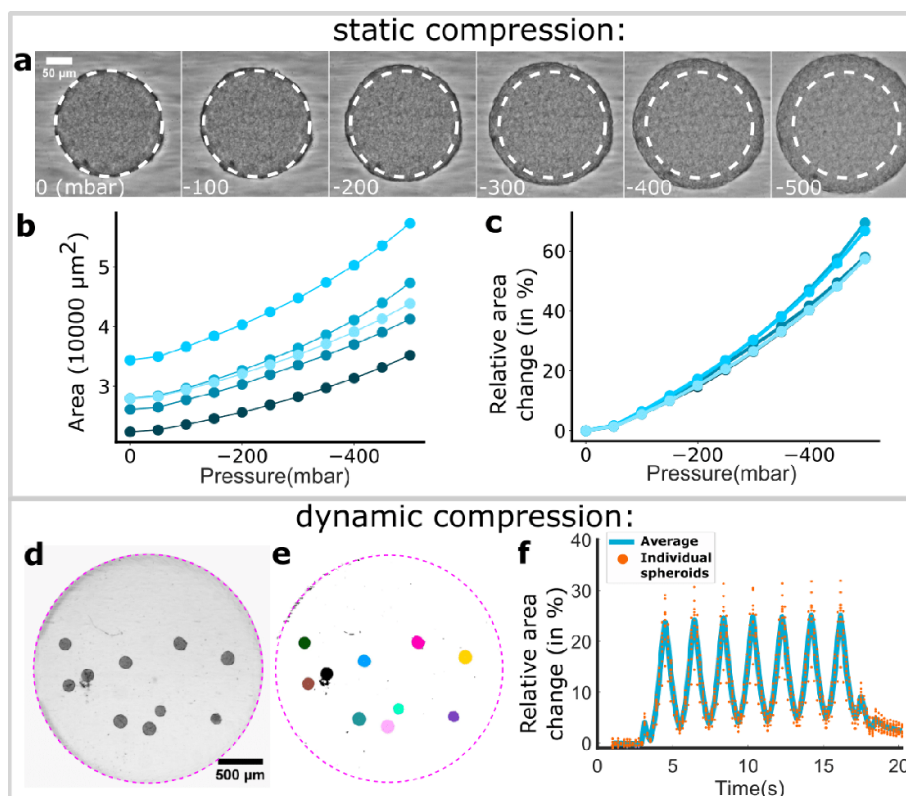


**Figure 3.** Measurements of static and dynamic spheroid compression. (a) Snapshots of a spheroid's compression as the air cavity pressure decreases. The pressure values are on the bottom left of each picture (in mbar). (b) For five spheroids in the same chip (each curve is one spheroid), values of the measured equatorial area as a function of the pressure inside the control chamber. (c) For the same spheroids as (b), change in the equatorial area as a function of the pressure inside the control chamber. (d) Spheroids are trapped inside the disc region of the observation chamber. (e) Automatic segmentation of the individual spheroids shown in panels (c). (f) Dynamic change of spheroids' areas (in panels (c) and (d)) during a sinusoidal pressure cycle of maximum pressure 0 mbar, minimum pressure  $-300$  mbar, and frequency 0.5 Hz.

In the static compression mode, the ceiling is lowered stepwise, and we wait 5–10 s for the spheroids to reach a steady state at each step before taking an image (see movie 4). The observed area of the spheroids increases as a convex function of the applied pressure, independently of the initial undeformed area within the range tested here (see figures 3(b) and (c)). Moreover, by normalising the deformed area by its value at zero deformation, the curves are found to nearly collapse on a single master curve, where the  $\approx 10\%$  variability between spheroids can be attributed to differences in position within the chamber (figure 3(c)).

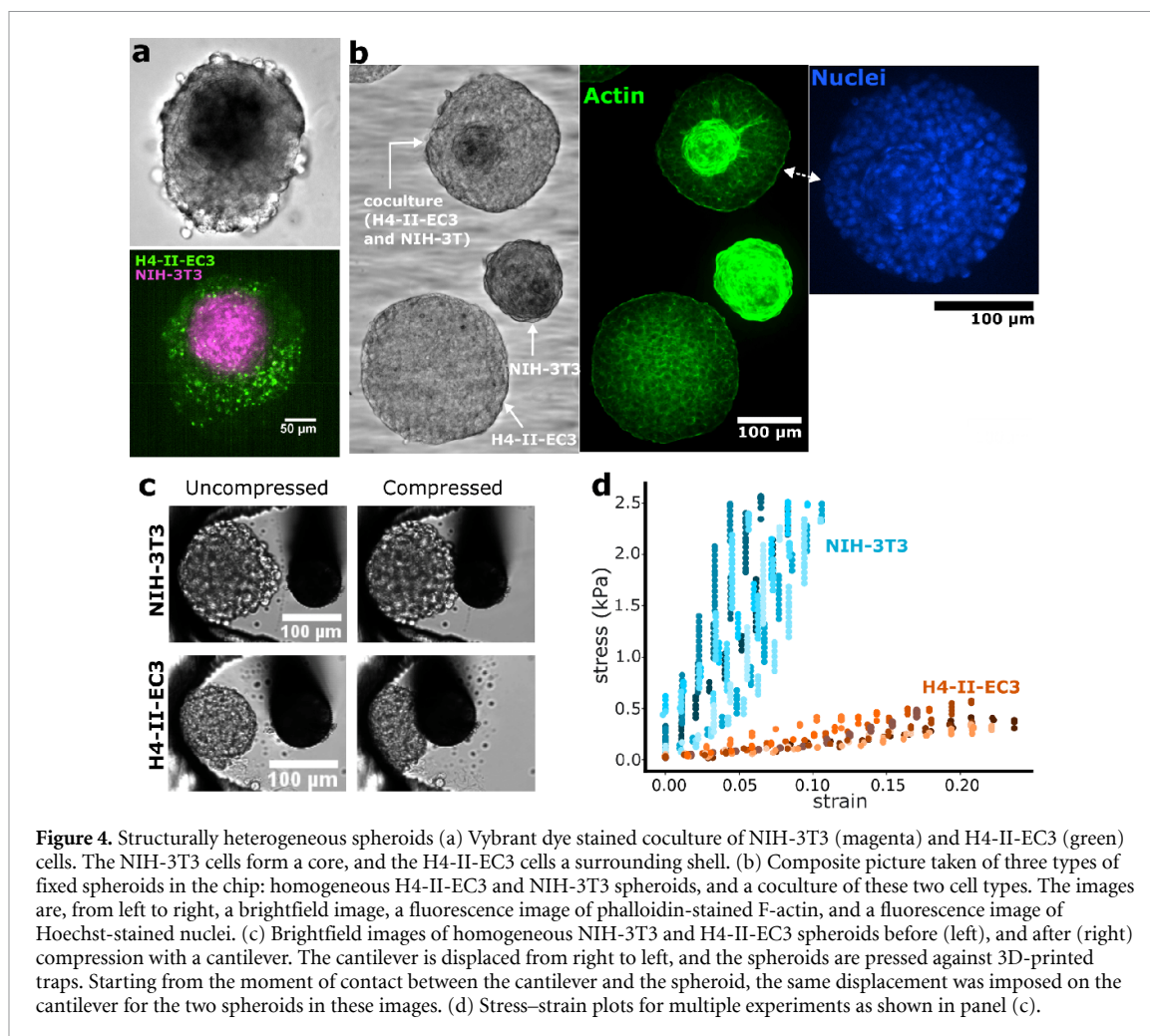
In addition to the static compression, the pressure in the air cavities can be programmed to follow a sinusoidal pattern. This in turn leads to oscillations of the chamber ceiling and of the observed area of the spheroids, as shown in figures 3(d)–(f) (SI movie 3). Here oscillations in the range 0,  $-300$  mbar, corresponding to a 25% deformation of the chamber, are applied at a frequency of 0.5 Hz. Again, the different spheroids follow the forcing frequency in synchrony, and they can be observed individually or together.

### 3. Measuring the stiffness heterogeneity within co-culture spheroids

The ability to apply a fixed deformation of the spheroids in this device can be used to probe the mechanics of these 3D tissues, by comparing quantitative image analysis with numerical simulations, as discussed below.

#### 3.1. Biological models and their characterisation off-chip

Co-culture spheroids were made by mixing H4-II-EC3 cells with fibroblasts (NIH-3T3). The result was reproducible core–shell structures where the fibroblasts formed a compact core, and the hepatoma cells formed a shell, as shown in figure 4(a). The core size was controlled with the initial number of seeded cells: NIH-3T3 cells do not proliferate in 3D while H4-II-EC3 cells do. The number of fibroblasts was therefore chosen to reach the desired core size and the number of hepatoma cells was chosen to reach a total diameter of  $130 \pm 20 \mu\text{m}$ .



Given the different phenotypes of these cell types, we expect their mechanical properties to be different. To investigate this, we look at the structure of the cocultures by staining their nuclei and F-actin. An early indication of the mechanical contrast between the two cell types can be found by the F-actin signal, which is much brighter in the fibroblasts than in the hepatoma cells (figure 4(b)) [22]. Moreover, the nuclear staining also displays a flattening of the fibroblast nuclei at the edge of the NIH-3T3 region, also suggesting that internal stresses are compressing these cells together.

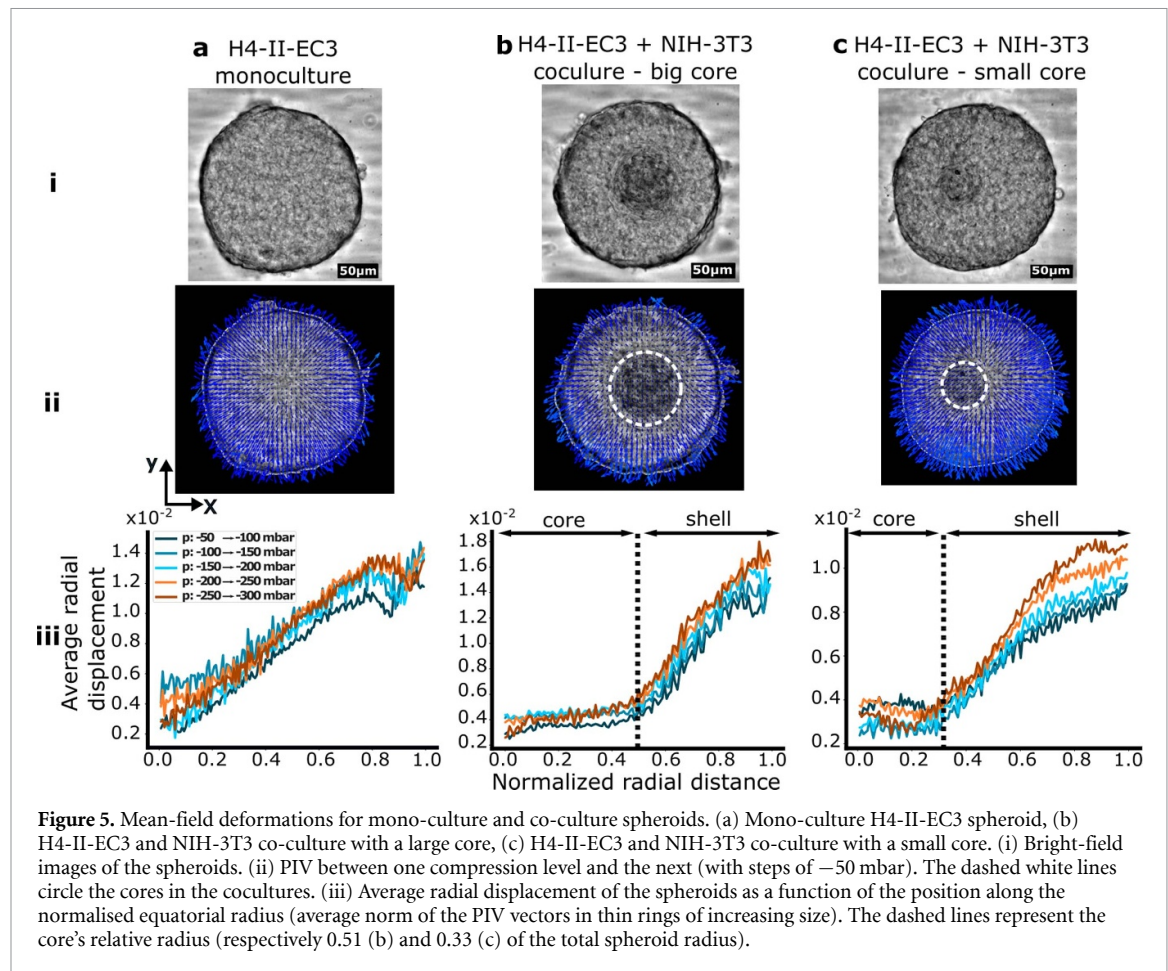
To confirm that the core and shell have different elastic moduli, we made mono-culture spheroids with the two cell types and measured their elastic response in a cantilever experiment: a micro-cantilever of known stiffness was used to press the spheroid against a 3D-printed trap while observing the spheroid in bright-field (see figure 4(c)). The difference between the imposed displacement on the root of the cantilever and the observed displacement of its tip was used to measure the deflection. The stress is  $f/A$  with  $f$  the applied force and  $A$  the contact area of the spheroid and the cantilever which we approximate  $A = 40 \times 40 \mu\text{m}^2$ . An ellipse was fit to the spheroid in each frame to measure the strain:

the change of the length of the semi-axis along the direction of the compression (for more detail, see 5.6). This allowed us to acquire the stress–strain plots of figure 4(d), which yield average apparent Young's moduli of  $E_{H4} = 2.14 \pm 0.69 \text{ kPa}$  and  $E_{3T3} = 31.8 \pm 9.08 \text{ kPa}$ , for the hepatomas and fibroblasts respectively.

### 3.2. Signature of the stiffness heterogeneity in the microfluidic device

The deformation of the mono-culture and co-culture spheroids was imaged using the micro-device while applying air cavity pressures from 0 to  $-300 \text{ mbar}$ , with steps of  $-50 \text{ mbar}$ . Brightfield images were taken while statically compressing mono-culture hepatoma spheroids and co-cultures with different fibroblast core sizes (figure 5 and SI movie 4). Consecutive images were compared together by applying a local image correlation algorithm, using a library for particle image velocimetry (PIV, see Methods section). This analysis provided a local displacement field on the spheroids, as shown in figure 5(i) for the transition from  $-100$  to  $-150 \text{ mbar}$  for three co-culture configurations.

The norm of the velocity vectors from this vector field can then be averaged azimuthally to obtain



a one-dimensional representation of the displacement as a function of the distance from the centre of each spheroid. This is shown in figure 5(iii) for the three spheroids in part (ii). A strong contrast is observed between the displacement field of the monoculture spheroid and the co-culture spheroids: in the first case, the displacement is continuous from the centre to the edge of the spheroid, while the co-culture cases display a flat region, with very little displacement. The undeformed region matches the observed fibroblast core for different core sizes.

### 3.3. Comparison with finite element simulations of a linear elastic model

Finite element simulations were used to better understand how differences between the mechanical responses of the core and the shell would influence the deformations of the whole co-cultures. Here the spheroids were modelled as nearly incompressible (Poisson ratio  $0.49$ ) elastic balls, deformed between two plane surfaces considered rigid, since the PDMS Young's modulus is  $100$ – $1000$  times higher than the values measured for our cell aggregates [23]. Contact between the spheroids and the substrate and ceiling surfaces is considered purely frictionless. Because of invariance properties, the problem depends only on

one spatial variable, here we choose the spheroid initial radius  $R$ , which we set to  $1$ , and normalise all other quantities with respect to it. By using the problem symmetries, this could be reduced to simulating an axisymmetric 2D section of a half hemisphere (figure 6(a)). In the simulated spheroid, the core and the shell were allowed to have different Young's moduli  $E_{\text{core}}$  and  $E_{\text{shell}}$ . Simulations were performed while varying  $E_r = E_{\text{core}}/E_{\text{shell}}$  and simulating the mesh's compression along  $z_s$  (figure 6(b)). Again, because of invariance properties, the problem only depends on this ratio, so we fix  $E_{\text{core}}$  to an arbitrary value and vary  $E_{\text{shell}}$ .

The displacement of the nodes along the  $x_s$  axis is plotted in figure 6(c) for a compressive strain of  $0.1R$ . This strain is comparable with the data of figure 5, where the deformation due to a  $50$  mbar pressure change is equivalent to approximately  $5 \mu\text{m}$  out of a channel height of  $100 \mu\text{m}$  (figure 5(iii)). The simulations produced a family of curves for different ratios  $E_r$  of the core to shell moduli, as shown in figure 6(c).

Comparison between the experimental and simulated displacement curves display semi-quantitative agreement for the monoculture spheroids, where the curve for  $E_r = 1$  presents a concave shape that reaches a displacement at the edge of around  $1.2\% \cdot R$ , in agreement with the experimental measurements of



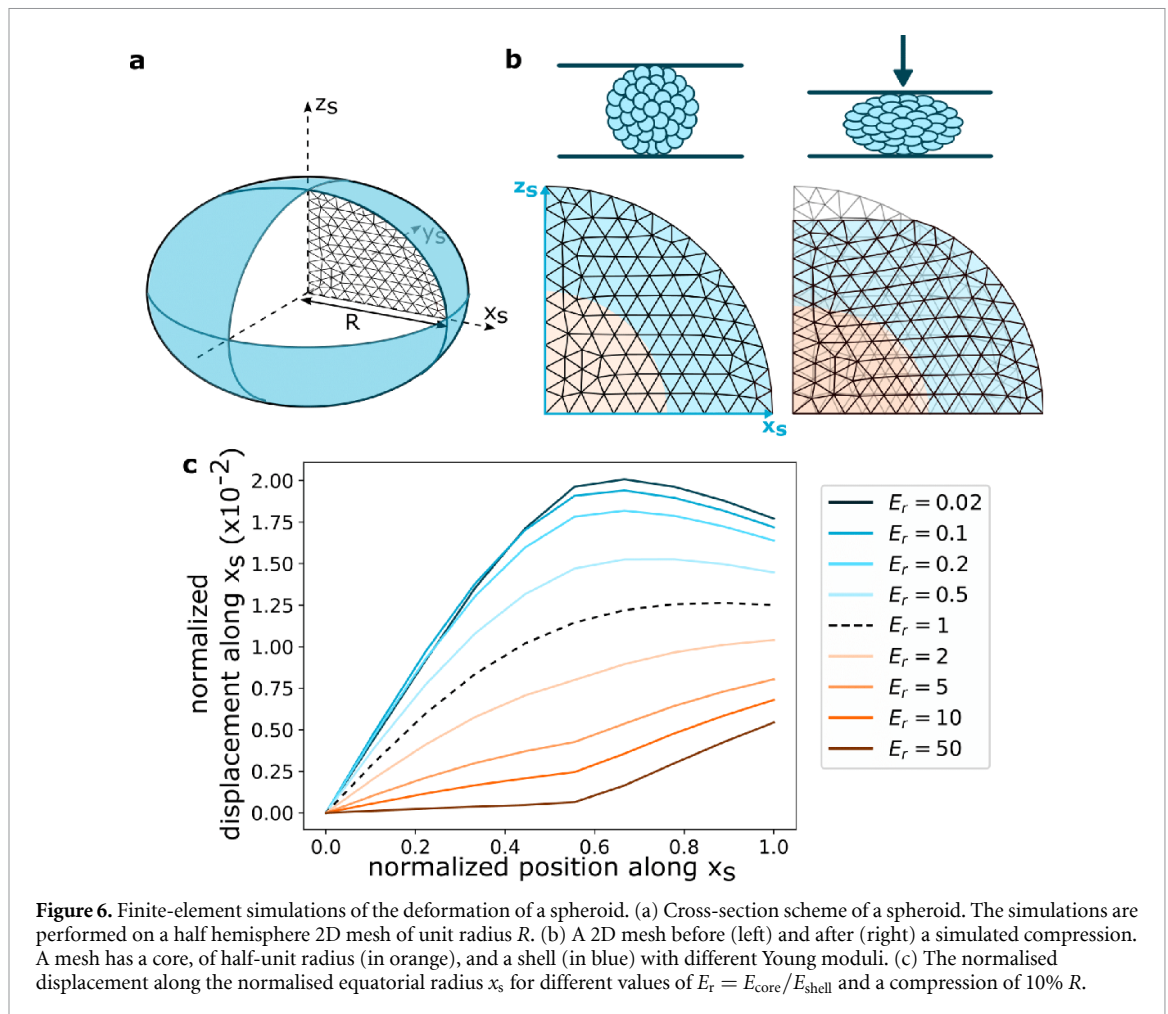


figure 5(a). In the case of the co-cultures however, the agreement is merely qualitative, with a factor of about 3 separating the values of the edge displacement between the experiments and simulations. Nevertheless the shape of the experimental displacement curve is consistent with a large heterogeneity in stiffness between the core and shell ( $E_r > 10$ ), which is in agreement with the independent measurements using the cantilever that give  $E_{r,exp} \approx 15$ .

#### 4. Discussion and outlook

In recent years the field of soft robotics has shown how the geometry of 3D structures could be leveraged to produce large and controlled deformations [24], namely by using pressurised channels to induce large deformations in elastomers [21]. Here we show that similar approaches of using pressure to deform an elastomeric micro-device can apply fine spatial and temporal control on the scale of a cell spheroid. Indeed, the ability of 3D printers to produce features with a large size contrast and with complex 3D shapes provides a unique opportunity to design micro-devices whose deformations can be tuned to a wide range of applications. From a practical point of view, the 3D printing step allows design iterations

to be made easily and enables different shapes to be tested. Finally, coupling this device with a programmable pressure source allows deformation to be controlled to the micron-scale and with the ability to reach frequencies that are much faster than biological times.

The device can be used to manipulate multicellular spheroids in several ways. The above measurements of mechanical heterogeneity within co-culture spheroids show that it is possible to obtain quantitative biophysical measurements from simple experimental protocols. The mechanical properties that are observed emerge from the organisation of the cells in the 3D structures. While they depend on the phenotype of the different cell types, they are only indirectly linked to the stiffness of individual cells in isolation. As such, the current measurements highlight the importance of working with multicellular structures rather than only with individual cells.

The current experimental and modelling approach suggest that the device can be used to perform more detailed measurements of the rheological properties of 3D tissues. However the current results suffer from two important limitations that will need to be addressed in future developments. First regarding the experimental setup, the current device lacks

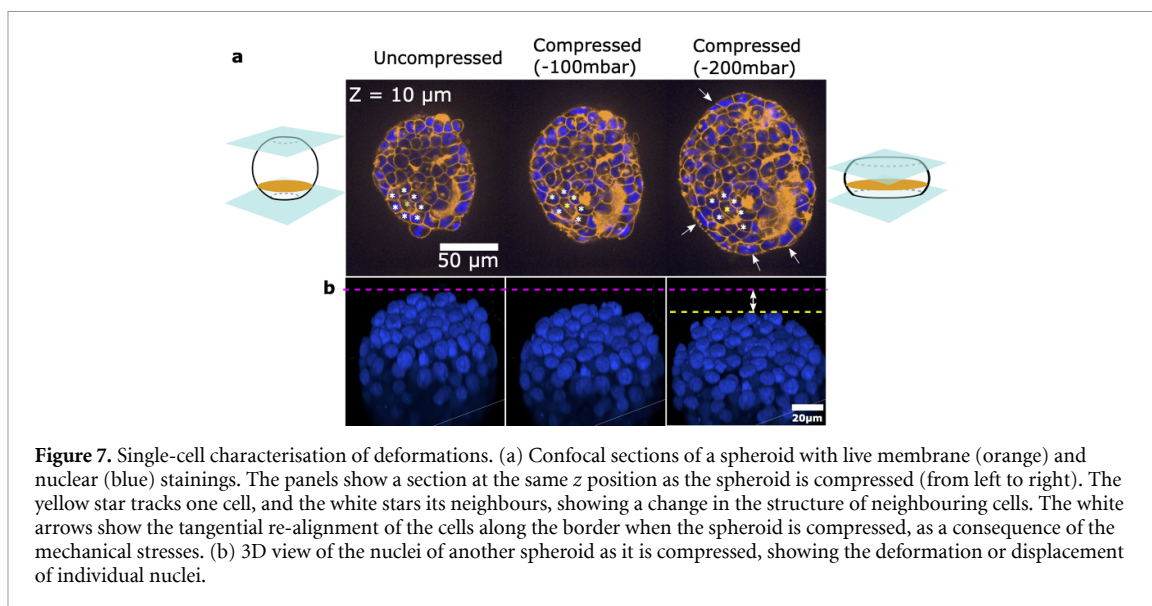


**Figure 7.** Single-cell characterisation of deformations. (a) Confocal sections of a spheroid with live membrane (orange) and nuclear (blue) stainings. The panels show a section at the same z position as the spheroid is compressed (from left to right). The yellow star tracks one cell, and the white stars its neighbours, showing a change in the structure of neighbouring cells. The white arrows show the tangential re-alignment of the cells along the border when the spheroid is compressed, as a consequence of the mechanical stresses. (b) 3D view of the nuclei of another spheroid as it is compressed, showing the deformation or displacement of individual nuclei.

the ability to measure the force that is being applied on the spheroids, in contrast with other parallel plate instruments that have been reported previously [25, 26]. As a result it is not currently possible to obtain a direct measurement of the stress–strain relationship of the spheroids; only relative stiffness values are observed here. Future versions of the technology will remedy this by combining the use of soft gels with the cell spheroids [12, 13, 15], in order to provide an *in situ* measurement of the applied force.

The second limitation concerns the numerical simulations shown here, which cannot capture the experimental results more quantitatively. Indeed, closer inspection of the deformation field in the experiments shows a lateral displacement of the core in the co-culture regime (SI movie 6), which breaks the azimuthal symmetry and therefore cannot be captured by the axisymmetric simulations. This symmetry breaking, which is likely to be due to inhomogeneities in the stiffness field within each of the two layers, is the reason why the simulations only qualitatively agree with the measurements of figures 5(b) and (c). It would therefore be very informative to develop more detailed numerical models, e.g. using cell-scale resolutions [27]. Quantitative comparisons between such models and experiments can then be used to solve the inverse mechanical problem in order to provide a detailed mapping of the stiffness field within complex 3D cultures.

When these future developments are combined with the ease of microfabrication and experimental protocols, it will be possible to study more complex tissues, such as stem-cell derived organoids that contain a wide diversity of cell types and where the cell patterning reflects their biological state [28]. Similar deformation analysis on complex tissues will be able to show the presence of anisotropic elastic moduli that may emerge e.g. due to the alignment of contractile muscle cells [29]. Beyond

simple measurements, the device can also be filled with hydrogels in order to guide the differentiation of cells within the spheroids, as was elegantly demonstrated recently [30].

Finally, going deeper into the biological questions will require the ability to link the mechanical stresses and biological response on multiple scales from individual cells to the complete tissue. Such a level of detail is critical since force transmission is inhomogeneous within 3D cellular structures, where individual cells may experience a wide variety of mechanical stresses under the action of external forcing. Indeed confocal images show that some cells within the aggregates get compressed while others rotate or get sheared (see figure 7 and SI movie 5). The ability to perform such highly-resolved images while applying the mechanical stimuli can then be combined with advanced image analysis and graph-based representations [31] in order to build multiscale models of mechanobiology [32].

## 5. Materials and methods

### 5.1. Fabrication of the compression device and setup

The moulds to fabricate the chips were designed using Fusion 360 (Autodesk) and 3D printed using an SLA-FORM3 printer and ClearV4 resin (Formlabs). The moulds were filled with a mixture of PDMS (SYLGARD, Dow) base and a curing agent at a ratio of 1:10. The PDMS was cured at 80 °C for 2 h. Then, it was separated from the moulds and then plasma treated (Cute, Femto Science Inc.) for 40 s. It was then bonded to a 24 × 65 mm (#1.5) coverslip (Menzel-Gläser). The device was connected to Fluigent's Flow EZ pressure controller (LU-FEZ-N800), fed by a supply line of −800 mbar. The pressure cycles were controlled using Fluigent's OxyGEN software

## 5.2. Cell culture and spheroid formation

H4-II-EC3 (CRL-1600, American Type Culture Collection) and NIH-3T3 cells (CRL-1658, American Type Culture Collection) between Passage 10 and Passage 20 were maintained on T-25 cm<sup>2</sup> flasks (Corning, France) in a standard CO<sub>2</sub> incubator (Thermo Fisher Scientific), following the instructions provided by the manufacturer (ATCC). The culture medium was composed of Dulbecco's Modified Eagle's medium (DMEM) containing high glucose (Gibco, Life Technologies) supplemented with 10% (v/v) fetal bovine serum (Gibco) and 1% (v/v) penicillin-streptomycin (Gibco). The cells were seeded at  $5 \times 10^4$  cells·cm<sup>-2</sup> and sub-cultivated every three days.

The spheroids were fabricated using ultra-low adhesion U-bottom 96 well plates (Corning). Monoculture of 300 H4-II-EC3 cells or 500 NIH-3T3 cells were seeded into the wells in order to form spheroids of about  $130 \pm 20$  μm in diameter after 24 h. To fabricate co-culture spheroids, the two cell types were mixed at different ratios to generate various sizes of fibroblast cores. 100 H4-II-EC3 and 400 NIH-3T3 cells resulted in large cores, while 200 cells of each cell type gave small cores. Co-cultures were grown for 72 h to ensure their proper core-shell arrangement by cellular self-organization.

## 5.3. Microscopy

All the images were taken using a motorized inverted microscope (Ti2, Eclipse, Nikon), equipped with either a spinning disc module (W1, Yokogawa) or an epifluorescence setup (Lumencor). Brightfield and fluorescent images were taken with a 20x objective with a 1.8 mm working distance (long working distance) and a 0.70 numerical aperture (NA) (CFI S Plan Fluor LWD, Nikon). The fluorescence images of figure 7 were taken with a 60x oil immersion objective with a 1.40 NA (Plan Apo VC, Nikon).

## 5.4. F-actin, membrane and nucleus staining

All the following reagents were introduced simply by placing a filled pipette tip at an inlet and letting the solution flow by gravity. No pressure is applied through the pipette, allowing the spheroids to stay in place. For F-actin staining, the cells were first fixed with a 4% (w/v) PFA (Alpha Aesar) for 30 min and permeabilized with 0.2 to 0.5% (v/v) Triton X-100 (Sigma-Aldrich) for 5 min. The samples were then blocked with a 5% (v/v) FBS solution and incubated for 90 min in a 1:200 phalloidin–Alexa Fluor 594 (Life Technologies) diluted in a 1% (v/v) FBS solution. The cytoplasmic membranes were stained with the CellBrite® Steady 650, following the manufacturer's protocol. The nuclei were labelled using the NucBlue™ Live ReadyProbes™ Reagent for live cells and NucBlue™ Fixed Cell ReadyProbes™ Reagent for PFA fixed cells, following the manufacturer's instructions.

## 5.5. Image analysis

The spheroids were segmented using a custom-made FIJI macro [33]. For each pressure value, the total area, perimeter, and major and minor axes of the spheroids are measured and recorded. To quantify radial displacement within spheroids upon compression, Particle Image Velocimetry (PIV) was performed using the open-source MatPIV toolbox in Matlab (2019b) [34], with a chosen window size  $32 \times 32$  px and overlap 75%. A displacement field was obtained for every deformation step applied to the spheroid by integrating the velocity data. Note that Digital Image Correlation (DIC) [35, 36] could have been used as an alternative to PIV to directly extract displacement data from the images.

## 5.6. Measurement of spheroid stiffness using cantilever

### 5.6.1. Cantilever fabrication and calibration

The cantilever consists of an 80 μm diameter flexible nitinol fibre (NitiWire, Fort Waynes Metals) attached to a solid L-shaped glass pipette (Sutter instrument), held in place using a pipette holder (Narishige). We calibrated the cantilever by measuring its horizontal deflection while adding small plasticine weights. A horizontally placed stereomicroscope monitored the deflection.

The computed stiffness of a cantilever of length  $l_{ref} = 14.5$  mm is  $k_{ref} = 0.2378$  mN·mm<sup>-1</sup>. Then, using beam theory, we can calculate the stiffness of any cantilever of a given length. The relation between the stiffness  $k$  and the length  $l$  is  $k = \frac{\tilde{k}}{l^3}$ , with  $\tilde{k}$  is a constant. We can then compute the constant  $\tilde{k}$  using our calibration values for  $k_{ref}$  and  $l_{ref}$ :  $\tilde{k} = k_{ref} l_{ref}^3 = 724.96$  mN·mm<sup>2</sup>.

### 5.6.2. Fabrication of traps for the spheroids

We fabricated traps to immobilize the spheroids during the measurement. The traps were 3D printed on coverslips using the DLP - Envisiontec Microplus HD printer. Before printing, the coverslips were silanized with 3-(Trimethoxysilyl)propyl methacrylate to prevent the resin traps from detaching.

### 5.6.3. Spheroid compression

Spheroids were immobilized against 3D-printed U-shaped traps and immersed in HBSS 1X at 20 °C (for less than 2 h). They were then compressed against the traps using a vertically mounted cantilever. The cantilever was brought near the spheroid using an XYZ manual micro-manipulator (Thorlabs), coupled to a piezoelectric stage (Physik Instrumente) controlled by a computer. We imposed a linear displacement on the cantilever to compress the spheroid (a 150 μm-displacement for H4-II-EC3 spheroids and a 300 μm-displacement for NIH-3T3 spheroids). We applied a speed of 2.5 μm·s<sup>-1</sup> for both cell types. We recorded the position of the cantilever and spheroid using a

confocal microscope (Zeiss LSM 980) with 2 s intervals between frames.

#### 5.6.4. Spheroid elasticity measurement

To compute the deflection of the cantilever tip, we measured the relative motion between the piezoelectric stage and the cantilever tip. The tip position was automatically tracked using a pattern recognition algorithm (`skimage.feature.match_template` from the Python Scikit-Image package [37]). The stage position was recorded by the stage hardware. The two sets of positions were synchronized using their absolute time, and the difference between the tip and stage positions was then computed at any time by linear interpolation. The zero-deflection was defined as the offset between the tip and stage positions when the cantilever is at rest before any movement. Any deviation to this offset is then considered a deflection. To measure the strain, an ellipse was manually fit in each frame to the spheroid. The strain in each frame is defined as  $\frac{l_f - l_0}{l_0}$ , with  $l_f$  the diameter of the ellipse semi-axis along the direction of the compression, and  $l_0$  the initial value of this diameter. The stress is  $f/A$  with  $f$  the applied force and  $A$  the contact area of the cantilever with the spheroid. We do not know this contact area but assuming it is similar for both kinds of spheroids, we approximate  $A = 40 \times 40 \mu\text{m}^2$ , based on the visible area on the images.

### 5.7. Numerical simulations

#### 5.7.1. Modeling device deformation

The ceiling's deformation was computed by solving a standard static load application problem in Autodesk FUSION 360. Finite element analysis of device deformation. The elastic modulus and the Poisson ratio of PDMS were input as, respectively,  $E_{PDMS} = 2$  MPa,  $\nu = 0.49$ . A zero displacement was imposed on the surface of the PDMS in contact with the glass slide. Negative pressure values from 0 to  $-500$  mbar were then applied in the control chamber. The software meshes the provided geometry automatically to determine the ceiling's deformation. For an air cavity pressure of  $-500$  mbar the simulation yields a maximum strain value of 0.27 in the PDMS. PDMS-10 (mixing ratio of base polymer to curing agent of 10 to 1) is known to remain in the elastic regime at such levels of strain [23]. The simulations were therefore linear.

#### 5.7.2. Modeling the mechanical response of hetero-spheroid compression

A standard linear elasticity model was solved by performing a finite element computation using the FEniCS library [38, 39] and the COMET demos [40]. Given the symmetry of spheroids and the considered compressive load, the system was reduced to an axisymmetric quarter disc section, as shown in figure 6(a). Therefore, we simulated the compression along the vertical axis on a mesh of such a 2D section

(figure 6(b)), and extracted the displacement of the nodes along the horizontal axis. Contact is enforced through a penalization approach, where the vertical position of the mesh boundary nodes is forced to be below a certain value. There is no constraint on the horizontal displacement, so the contact is purely frictionless. The deformability of the substrate and ceiling could be taken into account by adapting the penalty parameter. The mesh has a core and a shell of different Young's moduli  $E_{core}$  and  $E_{shell}$ . The input parameters were each Young's modulus, the size of the spheroid, the core radius, the Poisson ratio, the amplitude of the compression, and the node density in the mesh. Convergence tests were performed by using meshes with node distances between  $0.2R$  and  $0.01R$ . The node distance  $0.1R$  was chosen.

### Data availability statement

The 3D print design file of the device is available on GitHub: <https://github.com/BaroudLab/MechanoChip>. The data that support the findings of this study are openly available at the following URL/DOI: <https://doi.org/10.5281/zenodo.8428097>.

### Acknowledgments

The authors acknowledge support from the Biomaterials and Microfluidics platform and the FabLab at Institut Pasteur. Shirine Merlo is acknowledged for preliminary experiments on the deformable device. H B was partially funded by the Institut Pasteur Cancer Initiative. J G and A M acknowledge funding by ANR-19-CE13-0024-01. C N B acknowledges funding by ANR-23-CE30-0013-01 (Biomecanet).

### Author contributions

S J and C N B conceptualised the project. S J and H B conducted the device experiments and analysis. A M established the cantilever setup and A M, H B, S J conducted cantilever experiments and analysis. H B and M G performed numerical simulations. S J, H B, S S, A M and C N B wrote the manuscript. All authors read and discussed the manuscript.

### Conflict of interests





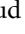
S J and C N B are named inventors on a patent application related to the results shown here. Other authors state no conflict of interest.

### ORCID iDs

Shreyansh Jain  <https://orcid.org/0000-0001-6754-000X>

Hiba Belkadi  <https://orcid.org/0009-0009-1116-5314>



Arthur Michaut  <https://orcid.org/0000-0003-1226-0021>  
 Sébastien Sart  <https://orcid.org/0000-0002-4720-4671>  
 Jérôme Gros  <https://orcid.org/0000-0002-2264-2851>  
 Martin Genet  <https://orcid.org/0000-0003-2204-201X>  
 Charles N Baroud  <https://orcid.org/0000-0001-5414-2010>

## References

- [1] Hannezo E and Heisenberg C-P 2019 Mechanochemical feedback loops in development and disease *Cell* **178** 12–25
- [2] Kim S, Uroz M, Bays J L and Chen C S 2021 Harnessing mechanobiology for tissue engineering *Dev. Cell* **56** 180–91
- [3] Beeghly G F, Amofa K Y, Fischbach C and Kumar S 2022 Regulation of tumor invasion by the physical microenvironment: lessons from breast and brain cancer *Annu. Rev. Biomed. Eng.* **24** 29–59
- [4] Alibert C, Goud B and Manneville J-B 2017 Are cancer cells really softer than normal cells? *Biol. Cell* **109** 167–89
- [5] Urbanska M, Muñoz H E, ShawBagnall J, Otto S R, DiCarlo D and Guck J 2020 A comparison of microfluidic methods for high-throughput cell deformability measurements *Nat. Methods* **17** 587–93
- [6] González-Cruz R, Fonseca V and Darling E 2012 Cellular mechanical properties reflect the differentiation potential of adipose-derived mesenchymal stem cells *Proc. Natl Acad. Sci.* **109** E1523–9
- [7] McBeath R, Pirone D M, Nelson C M, Bhadriraju K and Chen C S 2004 Cell shape, cytoskeletal tension and RhoA regulate stem cell lineage commitment *Dev. Cell* **6** 483–95
- [8] Wei S C *et al* 2015 Matrix stiffness drives epithelial-mesenchymal transition and tumour metastasis through a TWIST1-G3BP2 mechanotransduction pathway *Nat. Cell Biol.* **17** 678–88
- [9] Latorre E *et al* 2018 Active superelasticity in three-dimensional epithelia of controlled shape *Nature* **563** 203–8
- [10] Lisica A, Fouchard J, Kelkar M, Wyatt T P J, Duque J, Ndiaye A-B, Bonfanti A, Baum B, Kabla A J and Charras G T 2022 Tension at intercellular junctions is necessary for accurate orientation of cell division in the epithelium plane *Proc. Natl Acad. Sci.* **119** e2201600119
- [11] Jain S *et al* 2020 The role of single-cell mechanical behaviour and polarity in driving collective cell migration *Nat. Phys.* **16** 802–9
- [12] Campàs O, Mammoto T, Hasso S, Sperling R A, O'Connell D, Bischof A G, Maas R, Weitz D A, Mahadevan L and Ingber D E 2013 Quantifying cell-generated mechanical forces within living embryonic tissues *Nat. Methods* **11** 183–9
- [13] Dolega M E, Delarue M, Ingremeau F, Prost J, Delon A and Cappello G 2017 Cell-like pressure sensors reveal increase of mechanical stress towards the core of multicellular spheroids under compression *Nat. Commun.* **8** 1–9
- [14] Mohagheghian E, Luo J, Chen J, Chaudhary G, Chen J, Sun J, Ewoldt R H and Wang N 2018 Quantifying compressive forces between living cell layers and within tissues using elastic round microgels *Nat. Commun.* **9** 1878
- [15] Souchaud A, Boutillon A, Charron G, Asnacios A, Nous C, David N B, Graner F and Gallet F 2022 Live 3D imaging and mapping of shear stresses within tissues using incompressible elastic beads *Development* **149** dev199765
- [16] Guevorkian K, Colbert M-J, Durth M, Dufour S and Brochard-Wyart F 2010 Aspiration of biological viscoelastic drops *Phys. Rev. Lett.* **104** 218101
- [17] Boot R, Koenderink G and Boukany P 2021 Spheroid mechanics and implications for cell invasion *Adv. Phys. X* **6** 1978316
- [18] Mary G *et al* 2022 All-in-one rheometry and nonlinear rheology of multicellular aggregates *Phys. Rev. E* **105** 054407
- [19] Huh D, Matthews B D, Mammoto A, Montoya-Zavala M, Hsin H and Ingber D 2010 Reconstituting organ-level lung functions on a chip *Science* **328** 1662–8
- [20] Paggi C A, Venzac B, Karperien M, Leijten J C H and LeGac S 2020 Monolithic microfluidic platform for exerting gradients of compression on cell-laden hydrogels and application to a model of the articular cartilage *Sens. Actuators B* **315** 127917
- [21] Siéfert E, Reyssat E, Bico J and Roman B 2019 Bio-inspired pneumatic shape-morphing elastomers *Nat. Mater.* **18** 24–28
- [22] Shaway J H, Balakrishnan U L, Stuckenholz C and Davidson L A 2018 Multiscale analysis of architecture, cell size and the cell cortex reveals cortical F-actin density and composition are major contributors to mechanical properties during convergent extension *Development* **145** dev161281
- [23] Kim T K, Kim J K and Jeong O C 2011 Measurement of nonlinear mechanical properties of pdms elastomer *Microelectron. Eng.* **88** 1982–5
- [24] Jones T J, Jambon-Puillet E, Marthelot J and Brun P-T 2021 Bubble casting soft robotics *Nature* **599** 229–33
- [25] Forgacs G, Foty R A, Shafirir Y and Steinberg M S 1998 Viscoelastic properties of living embryonic tissues: a quantitative Study *Biophys. J.* **74** 2227–34
- [26] Wu P-H *et al* 2018 A comparison of methods to assess cell mechanical properties *Nat. Methods* **15** 491–8
- [27] Merkel M and Manning M 2017 Using cell deformation and motion to predict forces and collective behavior in morphogenesis *Semin. Cell Dev. Biol.* **67** 161–9
- [28] Sart S, Tomasi R F-X, Barizien A, Amselem G, Cumano A and Baroud C N 2020 Mapping the structure and biological functions within mesenchymal bodies using microfluidics *Sci. Adv.* **6** eaaw7853
- [29] Ruan J-L, Tulloch N L, Razumova M V, Saiget M, Muskheli V, Pabon L, Reinecke H, Regnier M and Murry C E 2016 Mechanical stress conditioning and electrical stimulation promote contractility and force maturation of induced pluripotent stem cell-derived human cardiac tissue *Circulation* **134** 1557–67
- [30] Alberto Paggi C A, Hendriks J, Karperien M and Gac S 2022 Emulating the chondrocyte microenvironment using multi-directional mechanical stimulation in a cartilage-on-chip *Lab Chip* **22** 1815–28
- [31] Ronteix G, Aristov A, Bonnet V, Sart S, Sobel J, Esposito E and Baroud C N 2022 Griottes: a generalist tool for network generation from segmented tissue images *BMC Biol.* **20** 178
- [32] Sart S, Tomasi R F-X, Amselem G and Baroud C N 2017 Multiscale cytometry and regulation of 3D cell cultures on a chip *Nat. Commun.* **8** 469
- [33] Schindelin J *et al* 2012 Fiji: an open-source platform for biological-image analysis *Nat. Methods* **9** 676–82
- [34] Sveen J 2004 An introduction to MatPIV v.1.6
- [35] Hild F and Roux S 2012 Comparison of local and global approaches to digital image correlation *Exp. Mech.* **52** 1503–19
- [36] Genet M, Stoeck C T, Deuster C L C and Kozerke S 2018 Equilibrated warping: finite element image registration with finite strain equilibrium gap regularization *Med. Image Anal.* **50** 1–22
- [37] Vander Walt S, Schönberger J L, Nunez-Iglesias J, Boulogne F, Warner J D, Yager N, Gouillart E and Yu. T 2014 scikit-image: image processing in python *Peer J.* **2** 453
- [38] Logg A and Wells G N 2010 DOLFIN: automated finite element computing *ACM Trans. Math. Softw.* **37** 1–28
- [39] Logg A, Wells G and Hake J 2012 DOLFIN: a C++/Python finite element library *Automated Solution of Differential Equations by the Finite Element Method: The Fenics Book, Lecture Notes in Computational Science and Engineering* ed A Logg, K-A Mardal and G Wells (Springer) pp 173–225
- [40] Bleyer J 2018 Numerical tours of computational mechanics with FEniCS